Journal of Fluids and Structures 22 (2006) 371–390

JOURNAL OF
FLUIDS AND
STRUCTURES

www.elsevier.com/locate/jfs

Numerical simulation of viscous flow around unrestrained cylinders

G.X. Wu*, Z.Z. Hu

Department of Mechanical Engineering, University College London, London WC1E7JE, UK

Received 1 March 2005; accepted 11 December 2005
Available online 28 February 2006

Abstract

A 2-D analysis is made for the dynamic interactions between viscous flow and one or more circular cylinders. The cylinder is free to respond to the fluid excitation and its motions are part of the solution. The numerical procedure is based on the finite volume discretization of the Navier–Stokes equations on adaptive tri-tree grids which are unstructured and nonorthogonal. Both a fully implicit scheme and a semi-implicit scheme in the time domain have been used for the momentum equations, while the pressure correction method based on the SIMPLE technique is adopted to satisfy the continuity equation. A new upwind method is developed for the triangular and unstructured mesh, which requires information only from two neighbouring cells but is of order of accuracy higher than linear. A new procedure is also introduced to deal with the nonorthogonal term. The pressure on the body surface required in solving the momentum equation is obtained through the Poisson equation in the local cell. Results including flow field, pressure distribution and force are provided for fixed single and multiple cylinders and for an unrestrained cylinder in steady incoming flow with Reynolds numbers at 200 and 500 and in unsteady flow with Keulegan–Carpenter numbers at 5 and 10.

Keywords: Tri-trees; Adaptive remeshing; Finite volume method; Unrestrained cylinders; Navier–Stokes equation

1. Introduction

There are many engineering applications where fluid flow and body motion are fully coupled. One of these examples is a marine structure in water waves. The body is set into motion by the incoming waves or current and as a result more waves will be generated by the motion. The interaction is usually fully nonlinear and completely coupled. In other words, the body motion will depend on the wave and the wave structure in turn will depend on the motion. Such mutual dependence has been a big obstacle in analysis of nonlinear water wave and floating body interaction. To overcome this difficulty, Wu and Eatcok (1996, 2003) developed a procedure by introducing some auxiliary functions. Potential flow theory was used, as the effect of viscosity is not significant in the cases they considered. The use of auxiliary functions

---

*Corresponding author. Tel.: +44 20 7679 3870; fax: +44 20 7388 0180.
E-mail address: gx_wu@meng.ucl.ac.uk (G.X. Wu).

0889-9746/$ - see front matter © 2006 Elsevier Ltd. All rights reserved.
doi:10.1016/j.jfluidstructs.2005.12.002

allowed Wu and Eatock Taylor to obtain the body acceleration before the pressure distribution is known. Their method has been used in several other applications (Wu and Eatock, 2003; Wu et al., 2004; Wu and Hu, 2004) and has been found to be very effective.

For the viscous flow, the situation is more complex. In the present work, we consider a 2-D unrestrained cylinder in incoming flow, which means that the body is allowed to respond to hydrodynamic loading. The solution is based on the finite volume method together with an unstructured mesh generated through a tri-tree method (Hu et al., 2002). Several novel schemes are developed. Firstly, a new upwind method is introduced for the physical values on the cell face, which requires information only from the two cells sharing the face but with the order of accuracy higher than linear. Secondly, the nonorthogonal terms along the face are calculated from the derivatives at the centres of the two cells sharing the face. Thirdly, the pressure on the face attached to the body surface is obtained through the Poisson equation in the local cell. All these have significantly improved the scheme used previously (Hu et al., 2002), which allows a more realistic and complex simulation to be undertaken.

To tackle the nonlinear coupling between the body motion and the fluid loading, the coordinate system is fixed on the body. As a result, the body acceleration enters the governing equation. It is treated as part of the source term when solving the momentum equation, while the pressure correction equation based on the SIMPLE procedure remains the same. At each time step, the acceleration is assumed together with the velocity field and pressure distribution, taken from the solution at the previous time step for instance. During the iteration, the force on the body is calculated and the acceleration is updated. The iteration continues until the velocity field, pressure distribution and the body acceleration have all converged.

There is a large volume of work on flow interaction with cylinders. Much of it is, however, either for a fixed cylinder in steady or unsteady incoming flow, or for a cylinder undergoing forced oscillation in otherwise calm fluid. For a fixed cylinder in steady flow, Roshko (1954) and Wille (1960) provided experimental data at $\mathrm{Re} = 200$. Numerical simulations this case were undertaken by Lecointe and Piquet (1984), Franke et al. (1990), Chen et al. (1999) and Chan and Anastasiou (1999), together with cases at other Reynolds numbers. For a cylinder in forced motion or a fixed cylinder in an oscillatory flow, experimental studies and numerical simulations were undertaken by Hassan (1962), Bishop and Hassan (1964), Maull and Milliner (1978), Honji (1981), Bearman et al. (1985), Williamson (1985), Sarpkaya (1986), Obasaju et al. (1988), Tatauno and Bearman (1990), Kühtz (1996), Dütsch et al. (1998), Bothwick (1986), Stansby and Smith (1991), Wang and Dalton (1991), Lin et al. (1996), Zhang and Zhang (1997) and Baranyi (2003), Baranyi and Shirakashi (1999).

Here we shall first use our developed method to solve some of the problems in these publications for validation. The method is then used for other cases at different Reynolds and Keulegan–Carpenter numbers. Numerical results are provided for the velocity field through streamlines, pressure distributions, force histories and induced body motions.

2. Finite volume formulation for the Navier–Stokes equations

A Cartesian coordinate system $O-xy$ is defined. All the physical parameters are nondimensionalized by the density of the fluid ρ, a typical length of the body D and a typical velocity component U_0. Let ϕ represent either the velocity component u in the x direction or v in the y direction. The nondimensionalized Navier–Stokes equations for ϕ can be written as

$$\frac{\partial \phi}{\partial t} + \nabla(\mathbf{U}\phi) = \frac{1}{\mathrm{Re}}\nabla^2\phi - \frac{\partial p}{\partial x_m}, \tag{1}$$

where $\mathbf{U} = (u, v)$ is the velocity vector, p is the pressure, $m = 1$ corresponds to $\phi = u$ and $m = 2$ corresponds to $\phi = v$, and $(x_1, x_2) = (x, y)$. The Reynolds number is $\mathrm{Re} = U_0 D/\nu$ and ν is the kinematic viscosity of the fluid. To solve the problem, the fluid domain is divided into many small triangular cells. Integrating Eq. (1) over a cell V_i bounded by three surfaces A_{fj}, $j = 1, 2, 3$ (see Fig. 1), we have

$$\frac{\partial \phi}{\partial t} V_i + \sum_{j=1}^{3} (\mathbf{J} \cdot \mathbf{A})_{fj} = S^{\phi}, \tag{2}$$

where the flux vector $\mathbf{J}$ contains both the convection term and the diffusion term, and is defined as

$$\mathbf{J} = \mathbf{U}\phi - \frac{1}{\mathrm{Re}}\nabla\phi. \tag{3}$$

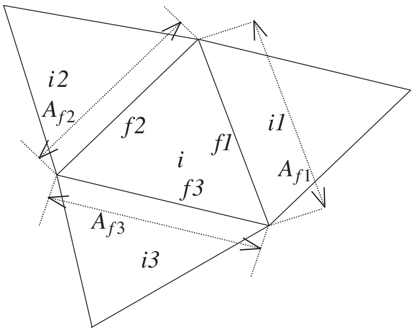

Fig. 1. A triangular element *i* with its three neighbours *i1*, *i2*, *i3*.

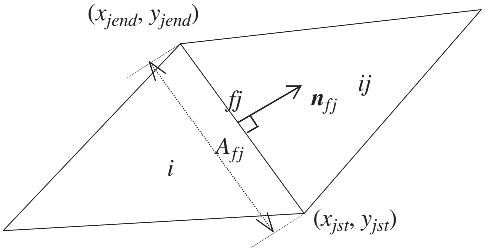

Fig. 2. Notation associated with face *fj*.

In Eq. (2), $\mathbf{A}_{fj} = \mathbf{n}_{fj} A_{fj}$ is the vector in the outward normal direction of face *fj* (see Fig. 2) and its magnitude is equal to the length of the face, and

$$S^{\phi} = -\int_{V_i} \frac{\partial p}{\partial x_m} \mathrm{d}V = -\sum_{j=1}^{3} (pAn_{x_m})_{fj} \tag{4}$$

is a source term to the equation, where n_{xfj} and n_{yfj} are the components of the normal of A_{fj} in the x and y directions, respectively. The convection term in Eq. (2) can be written as $\sum_{j=1}^{3} U_{fj} A_{fj} \phi_{fj}$, where

$$U^{fj} = u_{fj} \cdot n_{xfj} + v_{fj} \cdot n_{yfj}. \tag{5}$$

As the finite volume method defines the values at the centre of each cell, the face value ϕ_{fj} of is obtained through interpolation, or

$$\phi_{fj} = \lambda_j \phi_i + (1 - \lambda_j)\phi_{ij}, \tag{6}$$

where ϕ_i corresponds to cell *i* and ϕ_{ij} corresponds to cell *ij* (see Fig. 2). λ_i in Eq. (6) is the weighting function for linear interpolation, and it is defined as

$$\lambda_j = \frac{\sqrt{(x_{ij} - x_{fj})^2 + (y_{ij} - y_{fj})^2}}{\sqrt{(x_{ij} - x_i)^2 + (y_{ij} - y_i)^2}}, \tag{7}$$

where (x_{fj}, y_{fj}) are the coordinates of the intersection between face *fj* and the line linking points *i* and *ij*.

The second part of **J** in Eq. (3) represents diffusion. Across a given face *fj*, this becomes

$$-\frac{1}{\mathrm{Re}}(\mathbf{A} \cdot \nabla\phi)_{fj} = -\frac{1}{\mathrm{Re}}\left[A_{fj}\left(\frac{\partial \phi}{\partial x} n_x + \frac{\partial \phi}{\partial y} n_y\right)\right]_{fj}. \tag{8}$$

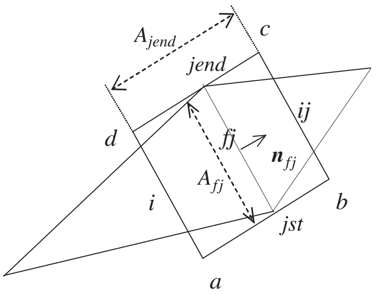

Fig. 3. Control volume for face *fj*.

To obtain the derivative on the face, we integrate Eq. (8) over a control volume bounded by the surface *a-b-c-d* (see Fig. 3), in which *bc* and *da* are parallel to the face, and *ab* and *cd* are parallel to the line linking *i* and *ij*. We have

$$-\frac{1}{\mathrm{Re}}\{\mathbf{A}\cdot\nabla\phi\}_{fj} = -\frac{A_{fj}}{\mathrm{Re}\,V_{fj}}\left[A_{fj}(\phi_{ij}-\phi_i)+A_{jend}(n_{xfj}n_{xjend}+n_{yfj}n_{yjend})(\phi_{jend}-\phi_{jst})\right], \tag{9}$$

where $(n_{xjend},\ n_{yjend})$ and A_{jend} are the normal vector and area of *cd*, respectively.

Substituting Eqs. (6) and (9) into Eq. (2), we obtain

$$a_p\phi_i = a_{f1}\phi_{i1}+a_{f2}\phi_{i2}+a_{f3}\phi_{i3}+S^{\psi}, \tag{10}$$

where

$$a_{fj} = -(1-\lambda_j)m_{fj}+K_{fj}, \tag{11}$$

$$a_p = b_{f1}+b_{f2}+b_{f3}+V_i/\Delta t, \tag{12}$$

$$b_{fj} = \lambda_j m_{fj}+K_{fj}, \tag{13}$$

$$K_{fj} = \frac{A_{fj}^2}{\mathrm{Re}\,V_{fj}}, \quad m_{fj} = U^{fj}A_{fj}, \tag{14}$$

$$S^{\psi} = S^{\phi}+\frac{1}{\mathrm{Re}}\sum_{j=1}^{3}\frac{A_{fj}}{V_{fj}}A_{jend}(n_{xfj}n_{xjend}+n_{yfj}n_{yjend})(\phi_{jend}-\phi_{jst})+\phi_i^{(0)}V_i/\Delta t, \tag{15}$$

and $\phi_i^{(0)}$ is the solution from the previous time step.

Eq. (10) is obtained based on a procedure similar to the central differencing technique used for the convection term. This provides good spatial accuracy but is prone to instability in the time domain. The stability of the solution scheme depends on the cell Reynolds number or the Peclet number which is the ratio of the product of the local velocity and the distance between cell centres divided by the kinematic viscosity. For the mesh used here, the Peclet number is given as $\mathrm{Pe} = m_{fj}/K_{fj}$. When Pe is larger than a critical value, say Pe_0, the upwind technique should be used. In the one-dimensional problem it can be shown that $\mathrm{Pe}_0 = 2$ for a grid with equal spacing. This number is used in this work.

In the previous applications (Hu et al., 2002), the upwind scheme is applied based on the QUICK scheme extended from that used for the structured mesh (Versteeg and Malalasekera, 1995). It may seem to be more accurate than the first-order method. But the QUICK scheme requires three points for interpolation. The third node will be on the face of the cell, which can be obtained only though another interpolation. Thus the originally intended accuracy may not be fully realized. Here a different upwind technique is developed. When $\mathrm{Pe}>\mathrm{Pe}_0$, instead of using Eq. (6), we write

$$\phi_{fj} = \begin{cases} \phi_i+\left(\frac{\partial\phi}{\partial x}\right)_i(x_{fj}-x_i)+\left(\frac{\partial\phi}{\partial y}\right)_i(y_{fj}-y_i), & U^{fj}>0, \\ \phi_{ij}+\left(\frac{\partial\phi}{\partial x}\right)_{ij}(x_{fj}-x_{ij})+(\frac{\partial\phi}{\partial y})_{ij}(y_{fj}-y_{ij}), & U^{fj}<0. \end{cases} \tag{16}$$

Eq. (10) will retain its form, but Eqs. (11) and (13) become

$$a_{fj} = \begin{cases} K_{fj}, & U^{fj} > 0, \\ -m_{fj} + K_{fj}, & U^{fj} < 0, \end{cases} \quad b_{fj} = \begin{cases} m_{fj} + K_{fj}, & U^{fj} > 0, \\ K_{fj}, & U^{fj} < 0. \end{cases} \tag{17}$$

In the case of $U^{fj} > 0$, a term $-[(\partial\phi/\partial x)_i(x_{fj} - x_i) + (\partial\phi/\partial y)_i(y_{fj} - y_i)]U^{fj}$ should be added to the source term, while in the case of $U^{fj} < 0$, $-[(\partial\phi/\partial x)_{ij}(x_{fj} - x_{ij}) + (\partial\phi/\partial y)_{ij}(y_{fj} - y_{ij})]U^{fj}$ should be added. These contributions to the source term are due to the second and third terms on the right-hand side of Eq. (16).

If face *fj* of the cell is on the boundary, a_{fj} and b_{fj} have to be modified, depending on the nature of the boundary condition. For the Dirichlet condition $\phi = \Phi$, we use $(\mathbf{A}\cdot\nabla\phi)_{fj} = A_{fj}(\Phi - \phi_i)/l$, where l is the distance from the centre of the cell to face *fj*. This leads to

$$b_{fj} = A_{fj}/(\mathrm{Re}\, l), \quad a_{fj} = 0.$$

The term corresponding to *fj* in the summation of Eq. (15) should be deleted because the control volume *a-b-c-d* adopted in Eq. (9) is no longer required on this surface. However, an additional term $[-m_{fj} + A_{fj}/(\mathrm{Re}\, l)]\Phi$ should be added to the source term due to the boundary condition. For the Neumman condition we have $\partial\phi/\partial n = 0$, $b_{fj} = m_{fj}$, $a_{fj} = 0$, and the term corresponding to *fj* in the summation of Eq. (15) should be deleted for the same reason as that in the Dirichlet condition.

The summation term in Eq. (15) is a result of the adoption of the nonorthogonal mesh. In the previous work (Hu et al., 2002), each nodal value in the term is obtained through the interpolation based on the distances of the node to the centres of those cells connected to this node. Here, we use

$$\phi_{jend} - \phi_{jst} = (-\phi_x n_y + \phi_y n_x)_{fj} A_{fj} = \{-[\lambda_j\phi_{ix} + (1-\lambda_j)\phi_{ijx}]n_{yfj} - [\lambda_j\phi_{iy} + (1-\lambda_j)\phi_{ijy}]n_{xfj}\}A_{fj}.$$

This requires information only from the two cells connected to the face *fj* and therefore is much easier to implement.

3. Pressure correction through the SIMPLE technique

Eq. (10) can be solved once the pressure is known. The difficulty is that pressure is part of the solution and is yet to be found. This is achieved through the use of the continuity equation. There are many possible ways of applying the continuity equation and the so-called SIMPLE algorithm of Patankar and Spalding (1972) is one of the most commonly used. It starts by assuming an initial pressure distribution p^+ with a velocity field ϕ^+. Eq. (10) can then be written as

$$a_p\phi_i^* = \sum_{j=1}^{3} a_{fj}\phi_{ij}^+ - \left(\frac{\partial p^+}{\partial x_m}\right)_i V_i + S, \tag{18}$$

where S contains the second- and third-order terms of Eq. (15). The new velocity field ϕ^* may not satisfy the required continuity equation. Thus a pressure correction p' is introduced, or

$$p = p^+ + p'. \tag{19}$$

Putting this into Eq. (18), we have

$$a_p\phi_i = \sum_{j=1}^{3} a_{fj}\phi_{ij}^+ - \left[\frac{\partial(p^+ + p')}{\partial x_m}\right]_i V_i + S. \tag{20}$$

Subtraction of Eq. (18) from Eq. (20) then gives

$$u_i = u_i^* - \frac{V_i}{a_p}\left(\frac{\partial p'}{\partial x}\right)_i, \tag{21}$$

$$v_i = v_i^* - \frac{V_i}{a_p}\left(\frac{\partial p'}{\partial y}\right)_i. \tag{22}$$

We require the new velocity field u_i and v_i to satisfy the continuity equation

$$\frac{\partial u}{\partial x} + \frac{\partial v}{\partial y} = 0, \tag{23}$$

which can be written as

$$\sum_{j=1}^{3} m_{fj} = \sum_{j=1}^{3} U^{fj} A_{fj} = 0 \tag{24}$$

after the integration over the cell is performed.

Substituting Eqs. (21) and (22) into Eq. (24) and using the control volume *a-b-c-d* to work out the derivatives of p', we have

$$a_i p'_i = a_{pf1} p'_{i1} + a_{pf2} p'_{i2} + a_{pf3} p'_{i3} + S_p, \tag{25}$$

where

$$a_{pfj} = \frac{A_{fj}^2 W_{fj}}{V_{fj}}, \tag{26}$$

$$a_i = a_{pf1} + a_{pf2} + a_{pf3}, \tag{27}$$

$$W_{fj} = \lambda_j \frac{V_i}{a_p} + (1-\lambda_j)\frac{V_{ij}}{(a_p)_{ij}}, \tag{28}$$

$$S_p = -\sum_{j=1}^{3} A_{fj} U^{*fj} + \sum_{j=1}^{3} \frac{A_{fj} W_{fj}}{V_{fj}} A_{jend}(n_{xfj} n_{xiend} + n_{yfj} n_{yjend})(p'_{jend} - p'_{jst}). \tag{29}$$

It should be noted that W_{fj} is from the term V_i/a_p in Eqs. (21) and (22) required on the cell face and therefore it is obtained through interpolation using the values of V_i/a_p of cell i and $V_{ij}/(a_p)_{ij}$ of cell ij.

When the velocity on face fj is given, U^{*fj} in Eq. (29) should be replaced by the known value while the term a_{pfj} in Eq. (25) together with the term corresponding to fj in the summation should be deleted, as no substitution of Eqs. (21) and (22) into Eq. (24) is required on this face. The nonorthogonal term in Eq. (29) is treated in the same way as that in the momentum equation, as discussed at the end of the last section.

Once the solution of Eq. (25) is found, Eqs. (21) and (22) are used to obtain the new velocity, or

$$u_i = u_i^* - \frac{1}{a_p}\sum_{j=1}^{3}(p' A n_x)_{fj} = u_i^* - \frac{1}{a_p}\sum_{j=1}^{3}(A n_x)_{fj}[(1-\lambda_j)p'_i + \lambda_j p'_{ij}], \tag{30}$$

$$v_i = v_i^* - \frac{1}{a_p}\sum_{j=1}^{3}(p' A n_y)_{fj} = v_i^* - \frac{1}{a_p}\sum_{j=1}^{3}(A n_y)_{fj}[(1-\lambda_j)p'_i + \lambda_j p'_{ij}], \tag{31}$$

and the new pressure distribution can be obtained from Eq. (19).

4. Treatment for pressure on the boundary

The boundary condition on the body surface for pressure usually cannot be explicitly given. In fact this would not be a problem in the solution procedure, if it were not required in Eq. (4). When face fj is on the body, the pressure on the cell face cannot be obtained through Eq. (6), since there is no cell inside the body. To obtain p_{fj} there, we apply a gradient to Eq. (1). Because of the continuity equation, we have

$$\frac{\partial}{\partial x}\left(u\frac{\partial u}{\partial x} + v\frac{\partial u}{\partial y}\right) + \frac{\partial}{\partial y}\left(u\frac{\partial v}{\partial x} + v\frac{\partial v}{\partial y}\right) = -\nabla^2 p. \tag{32}$$

Integrating this equation over the cell, we obtain

$$\sum_{j=1}^{3}\left(\frac{\partial p}{\partial n}\right)_{fj} A_{fj} = -\sum_{j=1}^{3}\left[\left(u\frac{\partial u}{\partial x} + v\frac{\partial u}{\partial y}\right)n_x + \left(u\frac{\partial v}{\partial x} + v\frac{\partial v}{\partial y}\right)n_y\right]_{fj} A_{fj}. \tag{33}$$

The derivative of the pressure on the face attached to the body surface can then be obtained, as those on the other two faces can be obtained from their corresponding control volumes. From the derivative and p_i, p_{fj} on the body surface can be obtained from the Taylor expansion.

For p', we expect $\partial p'/\partial x = \partial p'/\partial y = 0$ on the body surface from Eqs. (21) and (22), as the velocity is known and no correction is needed there. Thus the face value p'_{fj} on the body surface is equal to p'_i at the cell centre, which can then be used in Eqs. (30) and (31).

5. Algorithm for an unrestrained cylinder

When the body is unrestrained, we consider the case in which only translation is allowed, while the same procedure can be used when rotation is included. A coordinate system (ξ, η) fixed in the body is defined, which forms the following relation with (x, y):

$$x = \xi + c_x(t), \quad y = \eta + c_y(t), \tag{34}$$

where $c_x(t)$ and $c_y(t)$ are the displacements of the body in x and y directions, respectively. If we use the relative velocity,

$$(u', v') = (u - U_b, v - V_b), \tag{35}$$

where $U_b = \mathrm{d}c_x/\mathrm{d}t$ and $V_b = \mathrm{d}c_y/\mathrm{d}t$ are the velocities of the body, the momentum equation becomes

$$\frac{\partial u}{\partial t} + \nabla(\mathbf{U}u) = \frac{1}{\mathrm{Re}}\nabla^2 u - \frac{\partial p}{\partial \xi} - \frac{\mathrm{d}U_b}{\mathrm{d}t}, \tag{36}$$

$$\frac{\partial v}{\partial t} + \nabla(\mathbf{U}v) = \frac{1}{\mathrm{Re}}\nabla^2 v - \frac{\partial p}{\partial \eta} - \frac{\mathrm{d}V_b}{\mathrm{d}t}. \tag{37}$$

Here the primes on (u, v) have been dropped for convenience. If these two equations are compared with Eq. (1), it can be seen that there are additional source terms due to the body accelerations $A_x = \mathrm{d}U_b/\mathrm{d}t$ and $A_y = \mathrm{d}V_b/\mathrm{d}t$ which will be included in S^ψ in Eq. (10). It should be noted that the acceleration is not known, and it needs to be found through the solution. We use an iteration scheme.

It is evident that the body acceleration has to be found through the forces (F_D, F_L). We have, through the standard stress tensor τ_{xx}, τ_{xy} and τ_{yy},

$$F_D = \int_{S_B} (\tau_{xx} n_x + \tau_{xy} n_y)\,\mathrm{d}A = \int_{S_0} \left[\left(p - \frac{2}{\mathrm{Re}}\frac{\partial u}{\partial x}\right)\mathrm{d}y + \frac{1}{\mathrm{Re}}\left(\frac{\partial u}{\partial y} + \frac{\partial v}{\partial x}\right)\mathrm{d}x\right], \tag{38}$$

$$F_L = \int_{S_0} (\tau_{xy} n_x + \tau_{yy} n_y)\,\mathrm{d}A = \int_{S_0} \left[\left(-p + \frac{2}{\mathrm{Re}}\frac{\partial v}{\partial y}\right)\mathrm{d}x - \frac{1}{\mathrm{Re}}\left(\frac{\partial u}{\partial y} + \frac{\partial v}{\partial x}\right)\mathrm{d}y\right], \tag{39}$$

in which a clockwise sense is assumed for integration. The acceleration can then be found from

$$A_x = \frac{F_D}{M_b}, \quad A_y = \frac{F_L}{M_b}, \tag{40}$$

where M_b is the nondimensionalized body mass. When there is a restoring force proportional to the displacement, this equation should be written as

$$A_x = \frac{F_D - K_x c_x}{M_b}, \; A_y = \frac{F_L - K_y c_y}{M_b}, \tag{41}$$

where K_x and K_y are the stiffnesses in the x and y directions, respectively.

For the problem of interactions between a floating body and water waves based on potential flow, the fully nonlinear coupling between the force and the body acceleration also exists. The potential flow is, however, governed by the Laplace equation with no explicit reference to the acceleration. The acceleration therefore does not have a direct effect on the solution as it does not appear explicitly in the boundary condition on the potential either. The acceleration is required only when the pressure is needed through the Bernoulli equation. This is when the mutual dependence between the force and the acceleration appears explicitly. Neither of them is known in advance and both are part of the solution. For that problem, it is, however, possible to bypass the force and obtain the acceleration first by introducing some auxiliary functions (Wu and Eatock, 1996, 2003). It is, however, not straightforward to adopt a similar scheme here (of surface integration only), as the acceleration is in the governing equation. But the method proposed in this paper does not cause too much extra computational effort, as the iterative procedure for the acceleration is fully incorporated in that for the momentum equations and pressure correction equations. Once the governing equations for the fluid flow are solved, the acceleration is also found.

6. The solution procedure

The solution starts from the mesh generation which is based on a tri-tree procedure. The details are given in Hu et al. (2002). The method defines an initial equilateral triangle, within which the desired fluid domain will lie and it defines a set of seeding points about which the mesh will be generated. Consider each triangle in turn. If the triangle contains a seeding point, the triangle is divided. This procedure is repeated until the maximum division level is reached. All triangles are divided to a minimum level, and face regulation is applied to restrict the ratio of triangle sides sharing a common edge to 2:1. Hanging nodes are eliminated through further subdivision, and boundary treatment around the body is applied to move nodes of elements to the body surface. One of the advantages of this method is that all the information for a cell, including its neighbours, parents and children can be stored by means of an integer numbering system, which is particularly useful for the adaptive mesh.

Once the mesh is generated, the solution starts from an initial condition. As the vorticity develops with time, the grid may be adapted according to the magnitude of the vorticity as defined by the following equation:

$$\Omega_i = V_i \left| \frac{\partial u_i}{\partial y} - \frac{\partial v_i}{\partial x} \right|. \tag{42}$$

The values of $\Omega_{\max}$ and $\Omega_{\min}$ are specified. When $\Omega_i > \Omega_{\max}$, the element V_i is subdivided and when $\Omega_i < \Omega_{\min}$ the element is removed and the surrounding cells merge to become one. The index system of the mesh is then updated.

The solution procedure can be summarized as follows:

(a) generate the initial mesh based on the tri-tree method (Hu et al., 2002);
(b) initial velocity fields $u_i^{(0)}$ and $v_i^{(0)}$ at $t = 0$ are defined, which can be obtained from the potential flow for impulsively started motion (Batchelor, 1967, p. 471);
(c) the starting values for iteration at $t + \Delta t$ are taken from the solution at the previous time step;
(d) Eq. (10) is used to update u_i and v_i; the values of u_i and v_i required in a_p and a_{fj} are obtained from those at the previous iteration for the implicit scheme and from the previous time step for the semi-implicit scheme; when $\mathrm{Pe} \leqslant \mathrm{Pe}_0$, the central differencing method in Eq. (6) is used and when $\mathrm{Pe} > \mathrm{Pe}_0$, the upwind technique in Eq. (16) developed in this paper is used;
(e) Eq. (25) is used to obtainp', Eq.(19) is used to update the pressure, while Eqs. (30) and (31) are used to update the velocity; Eqs. (38) to (41) are used to obtain the body acceleration. If the new velocity value in the whole domain or the body acceleration is not sufficiently close to that at previous iteration, or p' is not sufficiently small, go back to (d);
(f) when the desired accuracy is achieved, go to (c) for calculation at next time step (apply mesh adaptation first if required at this time step).

7. Results

We focus our analysis here on circular cylinders. As discussed previously, the diameter of the cylinder D, and the fluid density ρ, have been used for nondimensionalization together with the velocity of the incoming stream or the amplitude of the oscillatory flow, which is U_0 in both cases. The computational configuration is shown in Fig. 4. The time step is taken as $\Delta t = 6.9 \times 10^{-3}$, as further reduction does not give a visible difference in the result. The solution is considered to have converged when the difference between the current result and that at the previous iteration in the momentum equation falls below 1.0×10^{-6} and the error in the continuity equation falls below 1.0×10^{-3}, or $\sum_{j=1}^{3} m_{fj}/V_i < 1.0 \times 10^{-3}$at every cell.

7.1. Fixed cylinders

A uniform incoming flow is from the left side of the domain. The cylinder is placed in the flow with $Le = 5D$, $Lr = 20D$ and $Ls = 10D$ (see Fig. 4). No-slip conditions are imposed on the cylinder surface. The Dirichlet boundary

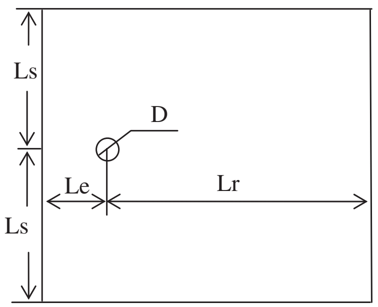

Fig. 4. Computational configuration.

Table 1
Grid convergence test for a cylinder at Re = 200

Case	Base grid				Adaptive grid at $t = 100$	
	Max. subdivision level	Min. subdivision level	No. of cells	No. of nodes	No. of cells	No. of nodes
1	12	6	10655	5554	18015	9234
2	13	6	15138	7914	22680	11685
3	14	6	23985	12573	31833	16497

Table 2
Drag and lift coefficients and Strouhal number for a cylinder at Re = 200

	C_D		C_L		S
	Max.	Min.	Max.	Min.	
Present result:					
Case 1	1.439	1.362	0.627	−0.629	0.193
Case 2	1.384	1.322	0.586	−0.582	0.190
Case 3	1.385	1.324	0.563	−0.564	0.190
Wille (1960) (experimental)	1.3 (mean)				
Roshko (1954) (experimental)					0.19
Williamson (1996) (experimental)					0.198
Franke et al. (1990)	1.31(mean)				0.194
Farrant et al. (2000)	1.37(mean)				0.196
Lecointe and Piquet (1984)	1.50	1.42	0.70	−0.70	0.23
Chen et al. (1999)	1.37	1.29	0.72	−0.72	0.20
Chan and Anastasiou (1999)	1.53	1.43	0.63	−0.63	0.18

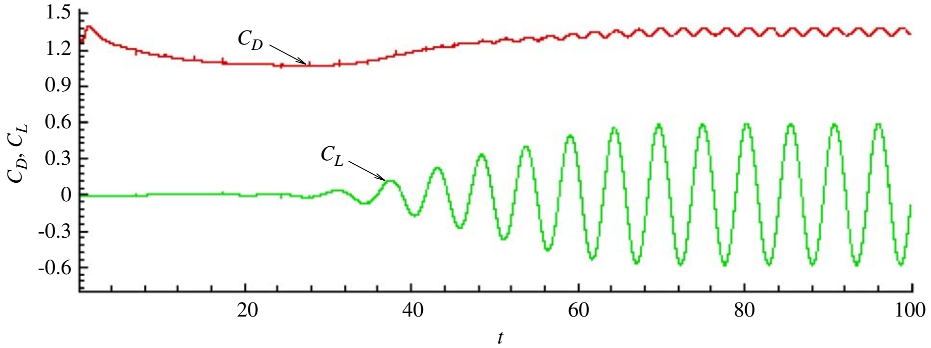

Fig. 5. The drag and lift coefficients on a cylinder with Re = 200.

condition is set for velocity at the inlet. The pressure at the outlet is prescribed, say $p = 0$, as a reference. Its exact value will not affect the flow and the force on the body. Elsewhere, the Neumann boundary condition is imposed.

The grid convergence tests are carried out for the case of $\mathrm{Re} = 200$, with base grids of maximum division level 12, 13 and 14, respectively, based on the procedure summarized in Section 6. The grid adaptation is applied with $\Omega_{\max} = 3.6 \times 10^{-3}$ and $\Omega_{\min} = 2.5 \times 10^{-4}$ and with a maximum level of 12 and minimum level of 6, which means no adaptation is applied even if the condition outlined after Eq. (41) is violated, when the division level has increased to the maximum or reduced the minimum. All these data are chosen through numerical tests based on the balance of the accuracy and the efficiency. Details of the numbers of elements, base grid nodes and the adapted grid nodes at $t = 100$ are listed in Table 1. Table 2 shows a comparison between the present results including the coefficients for the drag $C_D = \mathrm{Force}/(\frac{1}{2}\rho U_0^2 D) = 2F_D$ and the lift $C_L = \mathrm{Force}/(\frac{1}{2}\rho U_0^2 D) = 2F_L$, and the Strouhal number $S = f_v \cdot D/U_0$ ($f_v$is the vortex shedding frequency), and those obtained by experiment and other numerical simulations. The table shows that the error in the drag coefficient from levels 13 and 14 is about 0.07% while that in the lift is about 0.40%. These values are quite accurate for many practical

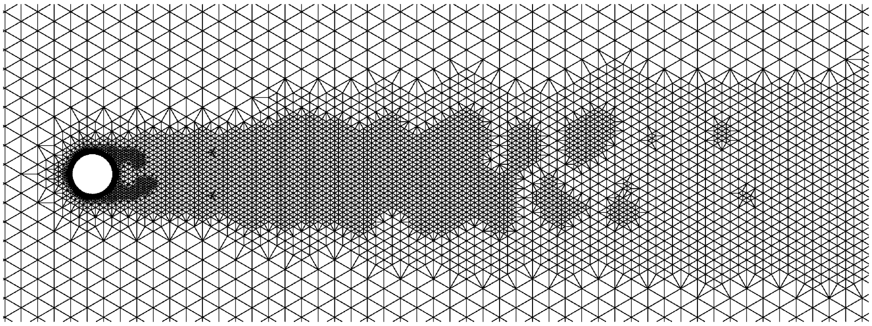

Fig. 6. Adaptive grid near the cylinder at $t = 62.50$ with $\mathrm{Re} = 200$.

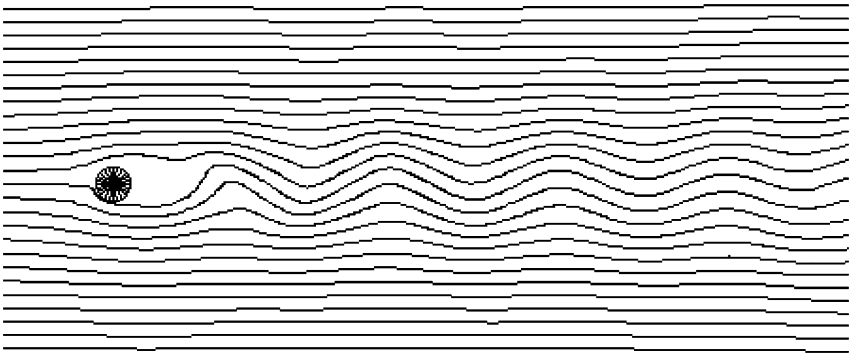

Fig. 7. Streamlines at $t = 62.50$ with $\mathrm{Re} = 200$.

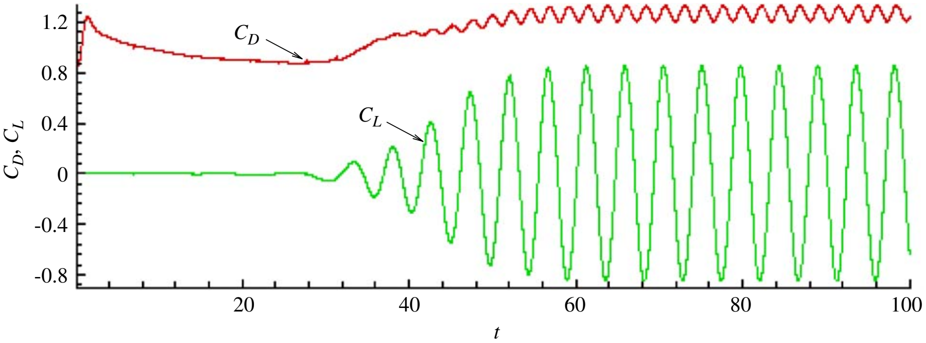

Fig. 8. The drag and lift coefficients on a cylinder with $\mathrm{Re} = 500$.

applications. The results are also in good agreement with the published data, although those from some numerical simulations are closer to the present result from the coarser mesh. The time history of the force is given in Fig. 5. The CPU required for case 3 is around 38 h, which corresponds to 9.68 s for each time step.

The adaptive grid near the cylinder at $t = 62.50$ is shown in Fig. 6. The densest distribution of elements is around the body, especially in a region behind the cylinder where the vorticities are strongest. Fig. 7 gives the streamlines with regular spacing $\Delta\psi = 4.0 \times 10^{-1}$, where ψ is the stream function. The oscillatory nature of the flow behind the cylinder is evident.

For the case of flow past a fixed cylinder at $\mathrm{Re} = 500$, the maximum division level of the base grid is 14 and rest of the parameters are the same as those in the previous case. The force history is given in Fig. 8. The mean value of C_D is lower

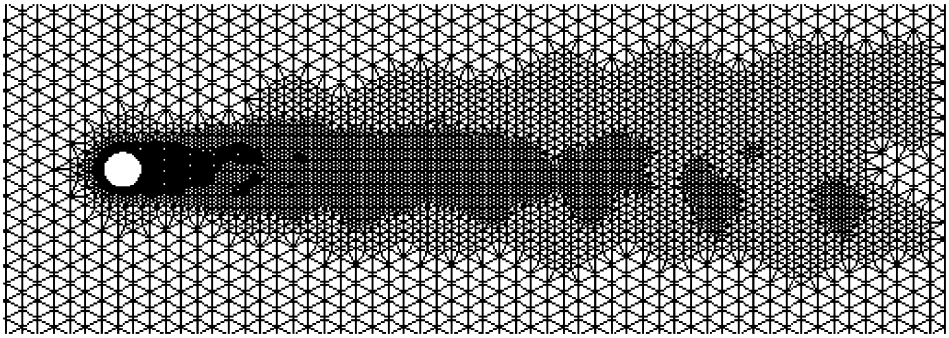

Fig. 9. Adaptive grid at $t = 62.50$ with $\mathrm{Re} = 500$.

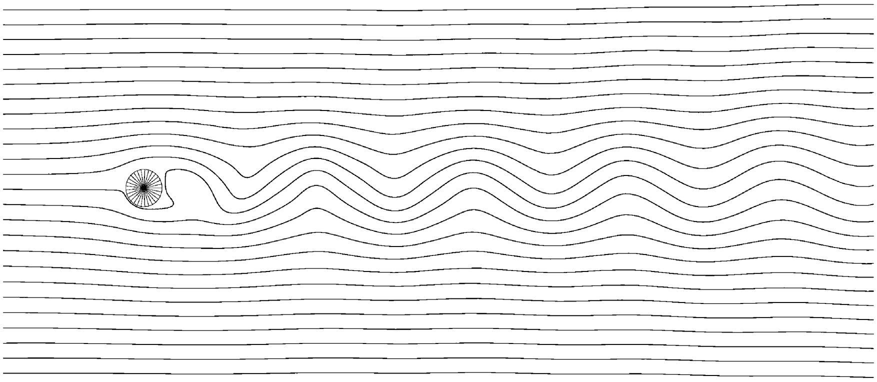

Fig. 10. Streamlines at $t = 62.50$ with $\mathrm{Re} = 500$.

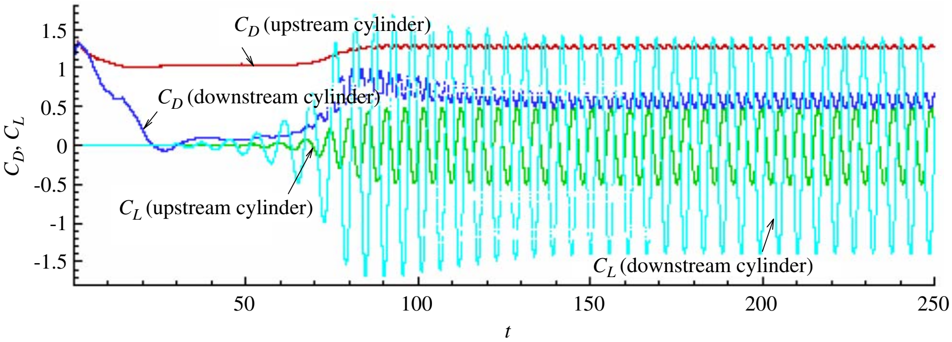

Fig. 11. The drag and lift coefficients for two cylinders in tandem ($c = G/D = 4$) with $\mathrm{Re} = 200$.

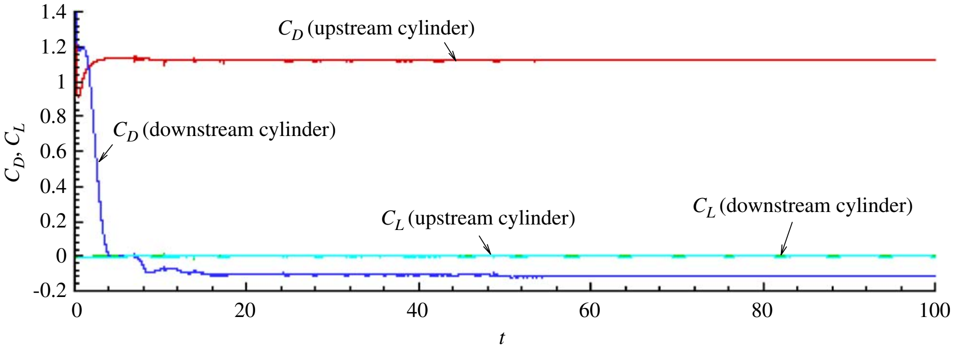

Fig. 12. The drag and lift coefficients for two cylinders in tandem ($c = 1$)with Re $=$ 200.

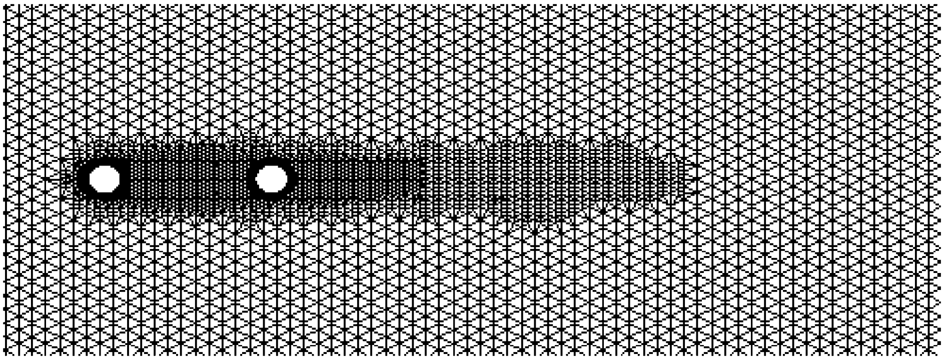

Fig. 13. Adaptive grid near two cylinders in tandem ($c = 4$) at $t = 62.50$ with Re $=$ 200.

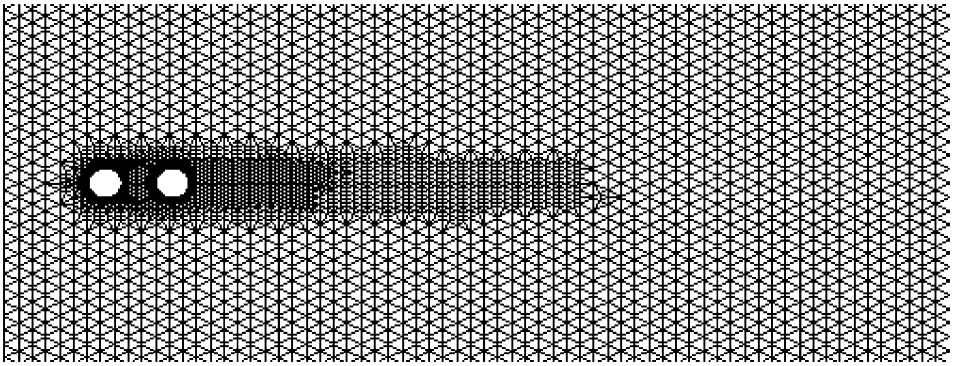

Fig. 14. Adaptive grid near two cylinders in tandem ($c = 1$) at $t = 62.50$ with Re $=$ 200.

than that at Re $=$ 200 but both the drag and lift here oscillate with a higher frequency and a bigger amplitude. Figs. 9 and 10 show the adaptive grid and streamlines with regular spacing $\Delta\psi = 4.0 \times 10^{-1}$ at $t = 62.50$. Comparing with the corresponding figures at Re $=$ 200, the vorticities at Re $=$ 500 are much stronger, which is of course expected.

Flow past two identical cylinders at Re $=$ 200 is considered next. The interaction between two cylinders depends on their relative position and the parameter $c = G/D$, where G is the minimum distance between the two cylinders, or the distance between the two centres minus the diameter. The drag and lift coefficients are shown in Fig. 11, which are obtained using a grid of level 14. Comparing with Fig. 5, we can see that the forces on the downstream cylinder take much longer to become periodic. The effect of the downstream cylinder on the upstream cylinder is, however, much

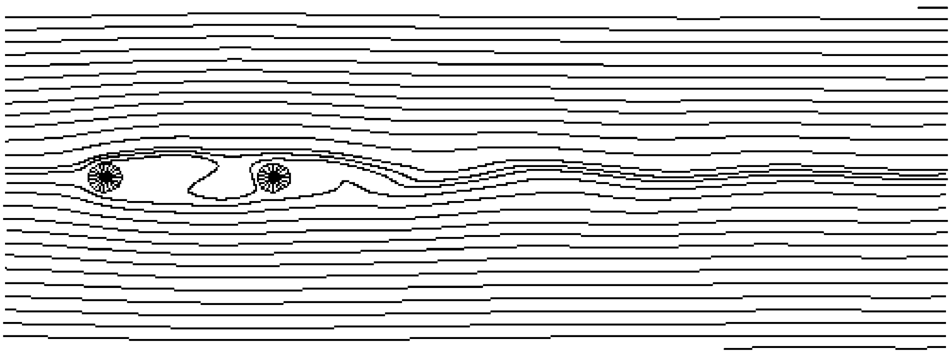

Fig. 15. Streamlines for two cylinders in tandem ($c = 4$) at $t = 62.50$ with $\mathrm{Re} = 200$.

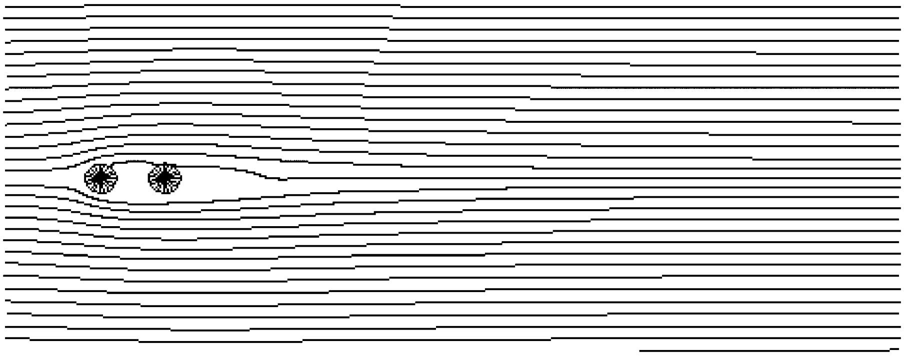

Fig. 16. Streamlines for two cylinders in tandem ($c = 1$)at $t = 62.50$ with $\mathrm{Re} = 200$.

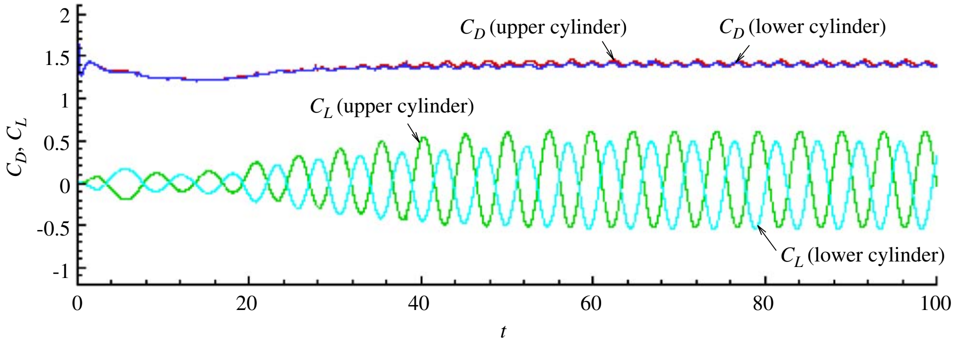

Fig. 17. The drag and lift coefficients for two cylinders side by side ($c = 4$)) with $\mathrm{Re} = 200$.

smaller. Fig. 12 gives the force history for the tandem case with $c = 1$. The oscillatory behaviour has virtually disappeared. The adaptive meshes used in these two cases at $t = 62.50$ are given in Figs. 13 and 14, and the streamlines are given in Figs. 15 and 16 with regular spacing $\Delta\psi = 4.0 \times 10^{-1}$. The figures show that the vorticity in these cases are far weaker than in the single cylinder case.

Figs. 17 and 18 give the force history for two cylinders side by side with $c = 4$ and 1, respectively. For the case with larger gap, the results remain more or less periodic, as in the single cylinder case. For the case of smaller gap, the results become more irregular. It is evident that interaction between the vortices behind two cylinders is much stronger in this case. Figs. 19 and 20 give the adaptive meshes and Figs. 21 and 22 provide the streamlines with regular spacing

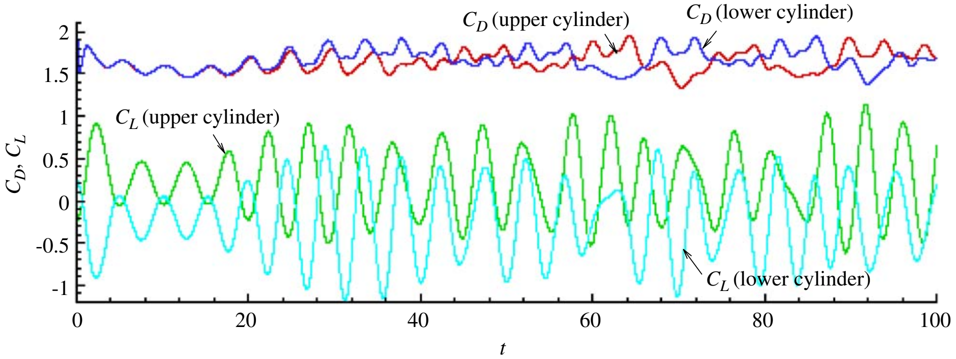

Fig. 18. The drag and lift coefficients for two cylinders side by side ($c = 1$)with Re $= 200$.

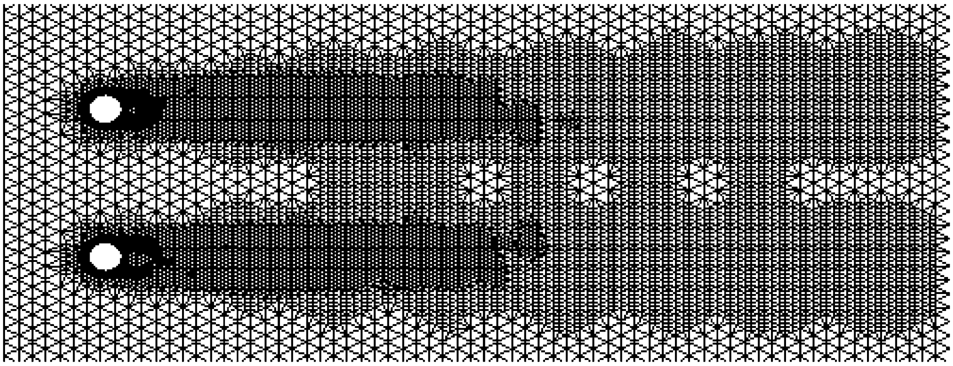

Fig. 19. Adaptive grid near two cylinders side by side ($c = 4$) at $t = 62.50$ with Re $= 200$.

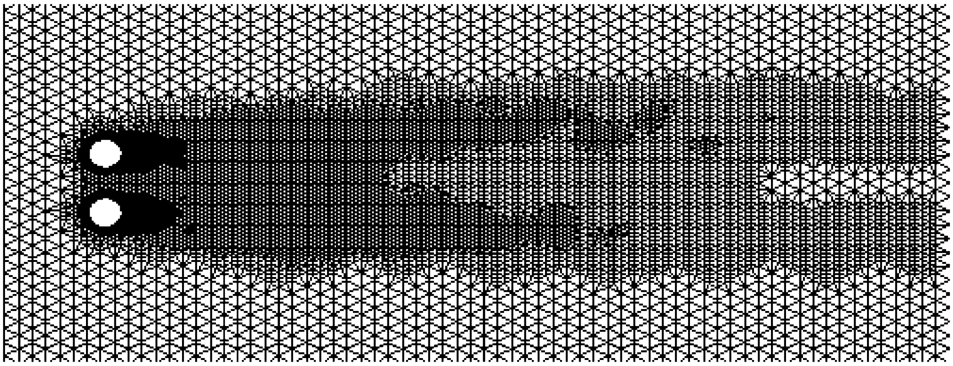

Fig. 20. Adaptive grid near two cylinders side by side ($c = 1$) at $t = 62.50$ with Re $= 200$.

$\Delta\psi = 4.0 \times 10^{-1}$ at $t = 62.50$. The case with $c = 4$ shows that the symmetry of the flow is held rather well, but it is totally destroyed in the case of $c = 1$.

7.2. Cylinder in forced oscillation

The cylinder is placed at the centre of the computational domain with $Le = 12.5D$ and $Lr = 12.5\,D$. The body undergoes forced oscillation with $U_0(t) = U_0 \cos \omega t$ in an otherwise quiescent fluid. The simulation is conducted in the

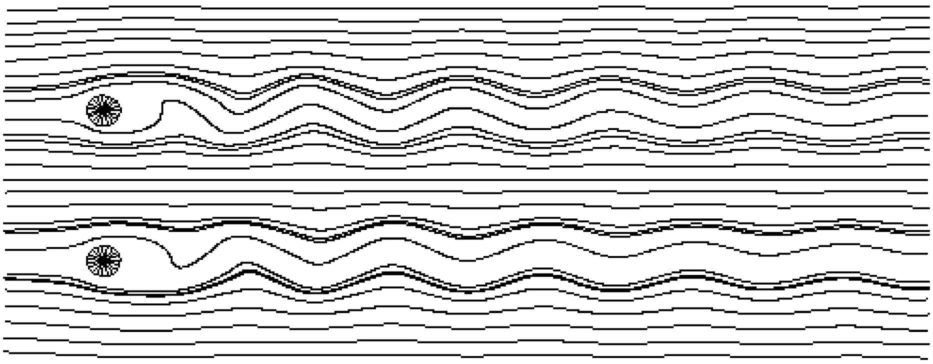

Fig. 21. Streamlines for two cylinders side by side ($c = 4$)at $t = 62.50$ with Re $= 200$.

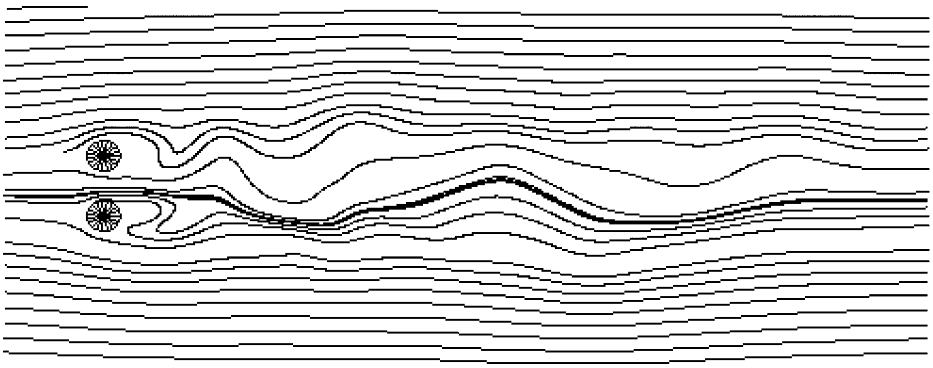

Fig. 22. Streamlines for two cylinders side by side ($c = 1$) at $t = 62.50$ with Re $= 200$.

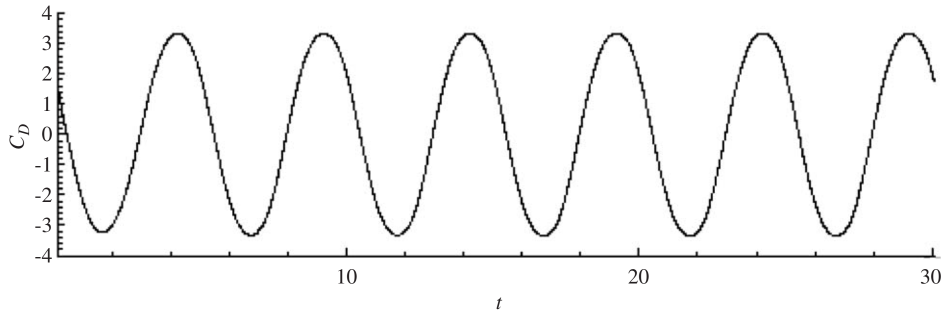

Fig. 23. The drag coefficient on the oscillatory cylinder with Re $= 200$ and KC $= 5$.

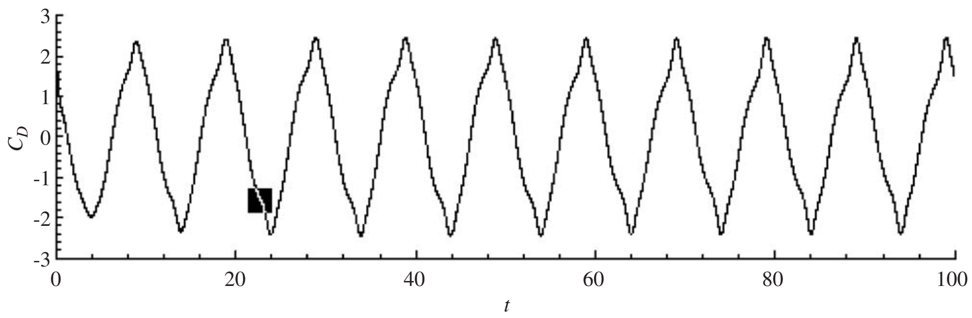

Fig. 24. The drag coefficient on the oscillatory cylinder with Re $= 200$ and KC $= 10$.

system fixed on the body. This is similar to the procedure in Section 5 but with known acceleration. The Reynolds number is now defined as $\mathrm{Re} = U_0 D/v$ based on the amplitude of the oscillation velocity and the Keulegan–Carpenter number is linked to the frequency through $\omega = 2\pi/\mathrm{KC}$. Fig. 23 gives the drag coefficient on the oscillatory cylinder for the case of $\mathrm{Re} = 100$ and $\mathrm{KC} = 5$ or $\beta = \mathrm{Re}/\mathrm{KC} = 20$. Figs. 24 and 25 show the drag and lift coefficients on the oscillatory cylinder for the case of $\mathrm{Re} = 200$ and $\mathrm{KC} = 10$ or $\beta = 20$. These results have been compared with those obtained by Dütsch et al. (1998). From their figure, the amplitude of the in-line force is found to be around 1.68 MN/m for the case with $\mathrm{Re} = 100$ and $\mathrm{KC} = 5$. This corresponds to C_D(amplitude) $= 3.33$ after nondimensionalization, which is in very good agreement with the result in Fig. 23.

7.3. Unrestrained cylinder in a steady approach flow

The computational domain used in this case is the same as that in Section 7.1 and the base mesh used is of a maximum level of 13. The simulation is carried out using the procedure outlined in Section 5. Figs. 26 and 27 show the

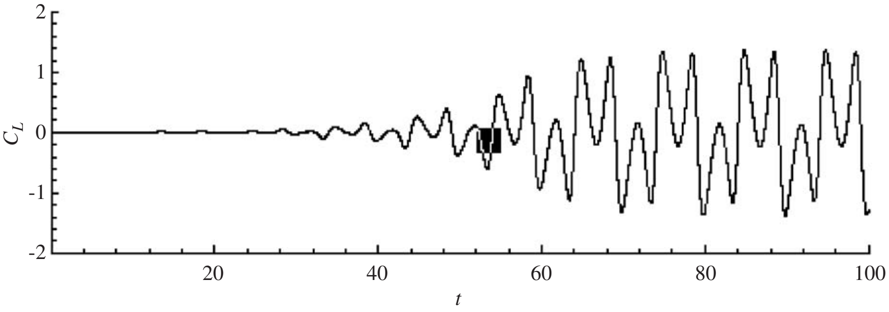

Fig. 25. The lift coefficient on the oscillatory cylinder with $\mathrm{Re} = 200$ and $\mathrm{KC} = 10$.

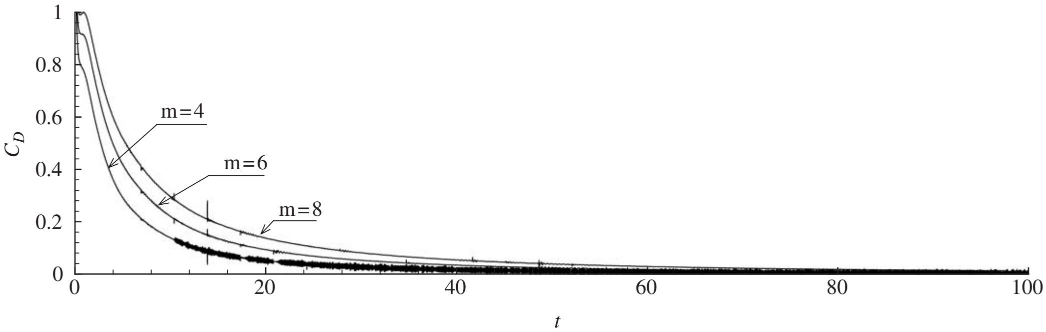

Fig. 26. The drag coefficient on unrestrained cylinders with different mass in steady flow with $\mathrm{Re} = 200$.

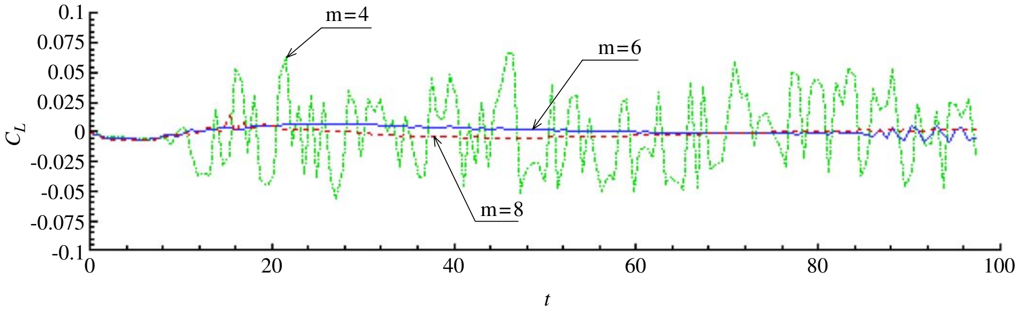

Fig. 27. The lift coefficient on unrestrained cylinders with different mass in steady flow with $\mathrm{Re} = 200$.

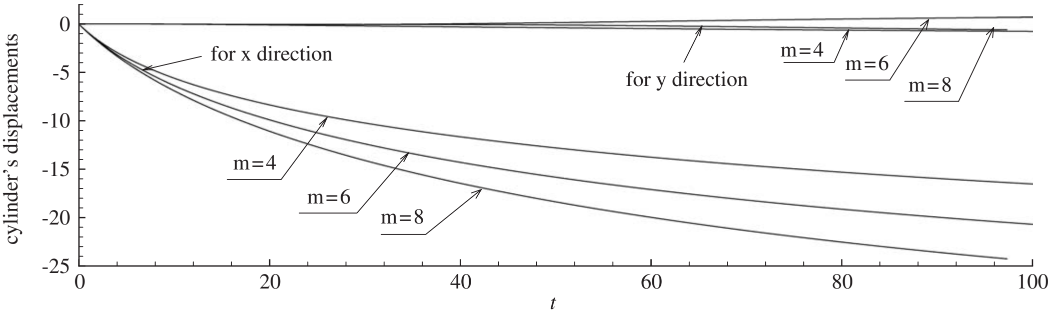

Fig. 28. Displacement of unrestrained cylinder with different mass in steady flow with $\mathrm{Re} = 200$.

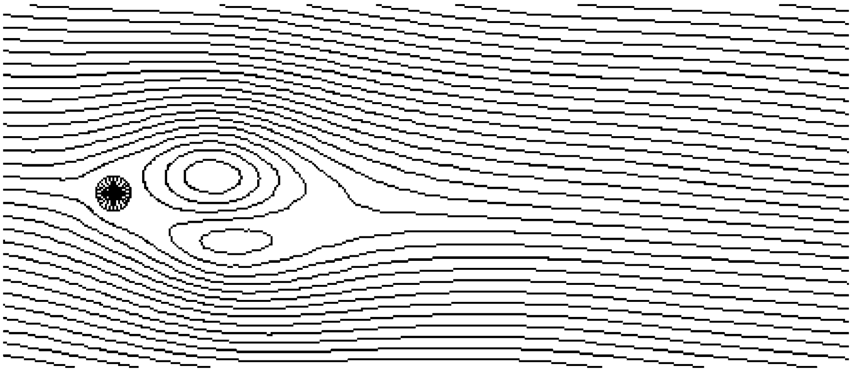

Fig. 29. Streamlines around an unrestrained cylinder ($m = 6$) in steady flow with $\mathrm{Re} = 200$ at $t = 62.50$.

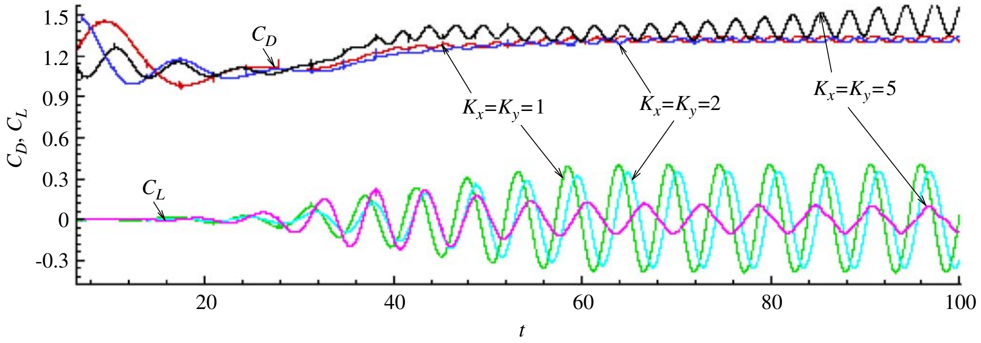

Fig. 30. The drag and lift coefficients on a cylinder with stiffness in steady flow with $\mathrm{Re} = 200$.

drag and lift coefficient, respectively, on a totally unrestrained cylinder at $\mathrm{Re} = 200$. The quantity m in the figure is defined as body mass$/0.25\rho\pi D^2$. The result shows that the force on the cylinder tends to zero. This is of course fully expected. In fact the problem is dynamically equivalent to an impulsively started cylinder in an otherwise stationary fluid. Due to viscosity, its motion will eventually come to a halt. There will be no motion and no force at the end, as shown in Fig. 28 where the displacement of the cylinder relative to the current becomes a constant and the relative velocity becomes zero. In fact the result in Fig. 28 is also the distance that the cylinder can travel in the otherwise stationary viscous fluid when it starts moving suddenly. The lift shown in Fig. 27 is quite small. The result may therefore be prone to numerical noise. The figure is plotted using the result after 100 time steps. Otherwise the plot would be highly oscillatory. It is also interesting to see that unlike the result in Section 7.1, the drag curve here has no obvious oscillation. This is because, before significant vortices have been developed, the relative motion between the body and the current has disappeared and the force has already become zero. This can be confirmed if comparison is made between the corresponding streamlines in Figs. 7 and 29.

When there is stiffness, it is not possible for the cylinder to drift away and oscillatory behaviour is expected. Fig. 30 shows the drag and lift, respectively, on a cylinder ($m = 6$) with stiffnesses $K_x = K_y = 1$, $K_x = K_y = 2$ and $K_x = K_y = 5$, respectively, and in a steady current with $\mathrm{Re} = 200$. Fig. 31 shows the displacements of the cylinder. The oscillation in the y direction is quite significant and it is far smaller in the x direction, although there is an evident drift from the original position. As the stiffness increases, the displacement in the x direction decreases and the system is more like a fixed cylinder. The behaviour in the y direction is more interesting. When $K_x = K_y = 5$, the lift is much smaller than in the other cases, but the displacement is much bigger. This can be explained by using the sinusoidal approximation for the force. Assuming $C_L = C_{L0}\sin(\omega t + \varepsilon)$ and $c_y = c_{y0}\sin(\omega t + \varepsilon)$, Eq. (41) gives

$$c_{y0} = \frac{2C_{L0}}{k_y - \omega^2 m\pi D^2/4}.$$

Using the results in Fig. 30, we obtain that $\omega = 1.160$, 1.175 and 0.990 corresponding to $K_x = K_y = 1$, $K_x = K_y = 2$ and $K_x = K_y = 5$, respectively. This leads to $k_y - \omega^2 M_b = -5.340, -4.506$ and 0.385, and $c_{y0} = -0.038$, -0.039 and 0.144. Thus the bigger displacement at $K_x = K_y = 5$ is due to the system being closer to resonance. In fact, Fig. 31 shows that the amplitude of the oscillation in this case still increases even at $t \approx 100$. Fig. 32 shows the streamlines with regular spacing $\Delta\psi = 4.0 \times 10^{-1}$ for the case of $K_x = K_y = 2.0$ and at $t = 62.50$. The strong vorticity in the wake can be seen, which is similar to the fixed cylinder rather than the fully unrestrained cylinder.

7.4. Unrestrained cylinder in an oscillatory flow

The cylinder in this case is placed in the middle of the computational domain, as shown in Section 7.2. Once again the Dirichlet boundary condition is set for the velocity at the inlet and the pressure at the outlet, while the Neumann

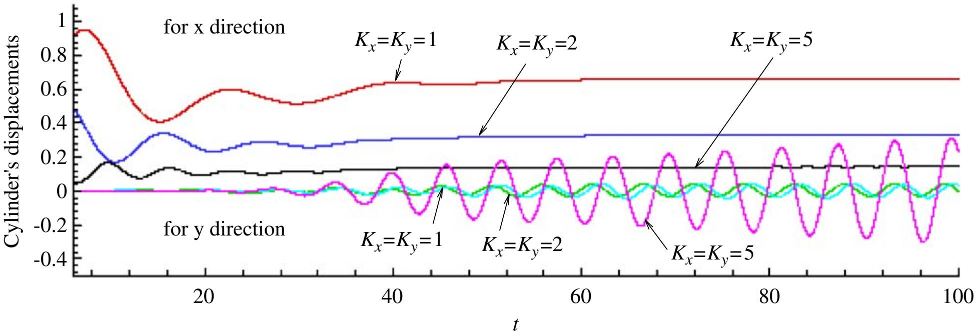

Fig. 31. Displacements of restrained cylinder ($m = 6$) in steady flow with $\mathrm{Re} = 200$.

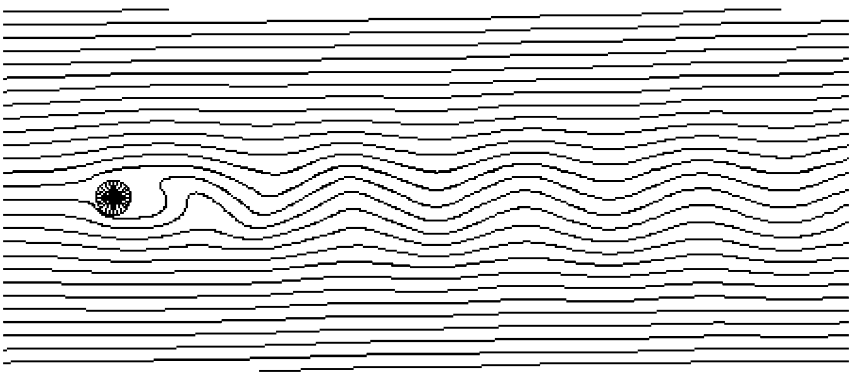

Fig. 32. Streamlines around a restrained cylinder with $K_x = K_y = 2$ ($m = 6$) in steady flow with $\mathrm{Re} = 200$ at $t = 62.50$.

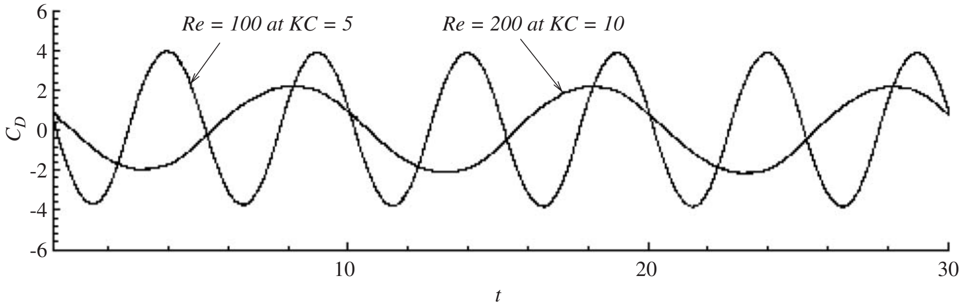

Fig. 33. The drag coefficient on an unrestrained cylinder ($m = 6$)in an oscillatory flow.

condition is imposed for the velocity at the outlet and the pressure at the inlet. The current is assumed as $U_0(t) = U_0 \cos \omega t$. The simulation is carried out based on the procedure discussed in Section 5, as the body acceleration is unknown. Fig. 33 shows the drag coefficient on the cylinder ($m = 6$) with $\mathrm{Re} = 100$ at $\mathrm{KC} = 5$ and $\mathrm{Re} = 200$ at $\mathrm{KC} = 10$, respectively. Unlike the result in Section 7.1, the drag here becomes periodic almost immediately. This is because the acceleration of the current plays a major role in Fig. 33, while the oscillatory behaviour in the steady incoming flow is due to the vorticity which takes time to develop.

8. Conclusions

A 2-D finite volume method together with a tri-tree grid has been applied to the problem of flow interactions with fixed and unrestrained cylinders. Several new numerical schemes have been developed including an upwind technique to calculate the face value using the information from the attached cells, a method to calculate the nonorthogonal terms and the treatment for the pressure on the cell face attached to the body. These schemes have significantly improved the quality of the numerical simulation. The time-stepping solution is found to be highly stable and the obtained results are in good agreement with those published previously from both experimental study and numerical simulation. The iterative scheme used in the paper to calculate the unknown body acceleration is also quite efficient for the cases considered, as it does not take significant amount of extra CPU. All these have laid a solid foundation for the method to be applied to more complex 2-D flow and for the method to be extended to 3-D cases.

Acknowledgements

The authors wish to thank Prof. Shijun Liao, Mr. Zhiliang Lin and Mr. Gang Guo of Shanghai Jiaotong University for their very helpful discussions.

References

Baranyi, L., 2003. Numerical simulation of flow past a cylinder in orbital motion. In: 12th International Conference on Fluid Flow Technologies, Hungary.

Baranyi, L., Shirakashi, M., 1999. Numerical solution for laminar unsteady flow about fixed and oscillating cylinders. Computer Assisted Mechanics and Engineering Sciences 6, 263–277.

Batchelor, G.K., 1967. An Introduction to Fluid Dynamics. Cambridge University Press, UK.

Bearman, P.W., Downie, M.J., Graham, J.M.R., Obasaju, E.D., 1985. Forces on cylinders in viscous oscillatory flow at low Keulegan–Carpenter numbers. Journal of Fluid Mechanics 154, 337–356.

Bishop, R.E.D., Hassan, A.Y., 1964. The lift and drag forces on a circular cylinder in a flowing fluid. Proceedings of the Royal Society London 277, 51–75.

Bothwick, A., 1986. Comparison between two finite-difference schemes for computing the flow around a cylinder. International Journal on Numerical Methods in Fluids 6, 275–290.

Chan, C.T., Anastasiou, K., 1999. Solution of incompressible flows with or without a free surface using the finite volume method on unstructured triangular meshes. International Journal on Numerical Methods in Fluids 29, 35–57.

Chen, Y.H., Yang, S.C., Yang, J.Y., 1999. Implicit weighted essentially non-oscillatory schemes for the incompressible Navier–Stokes equations. International Journal on Numerical Methods in Fluids 31, 747–765.

Dütsch, H., Durst, F., Becker, S., Lienhart, H., 1998. Low-Reynolds-number flow around an oscillating circular at low Keulegan–Carpenter numbers. Journal of Fluid Mechanics 360, 249–271.

Farrant, T., Tan, M., Price, W.G., 2000. A cell boundary element method applied to laminar vortex-shedding from arrays of cylinders in various arrangements. Journal of Fluids and Structures 14, 375–402.

Franke, R., Rodi, W., Schönung, B., 1990. Numerical calculation of laminar vortex shedding flow past cylinders. Journal of Wind Engineering and Industrial Aerodynamics 35, 237–257.

Hassan, A.Y., 1962. The effects of vibration on the lift and drag forces on a circular cylinder in a fluid flow. Ph.D. Thesis, University College, London.

Honji, H., 1981. Streaked flow around an oscillating circular cylinder. Journal of Fluid Mechanics 107, 347–367.

Hu, Z.Z., Greaves, D.M., Wu, G.X., 2002. Numerical simulation of fluid flows using an unstructured finite volume method with adaptive tri-tree grids. International Journal on Numerical Methods in Fluids 39, 403–440.

Kühtz, S., 1996. Experimental investigation of oscillatory flow around circular cylinder at low beta numbers. Ph.D. Thesis, Imperial College, London.

Lecointe, Y., Piquet, J., 1984. On the use of several compact methods for the study of unsteady incompressible viscous flow around a circular cylinder. Computer and Fluids 12, 255–280.

Lin, X.W., Bearman, P.W., Graham, J.M.R., 1996. A numerical study of oscillatory flow about a circular for low values of beta parameter. Journal of Fluids and Structures 10, 501–526.

Maull, D.J., Milliner, M.C., 1978. Sinusoidal flow past a circular cylinder. Coastal Engineering 2, 149–168.

Obasaju, E.D., Bearman, P.W., Graham, J.M.R., 1988. A study of forces, circulation and vortex patterns around a circular cylinder in oscillating flow. Journal of Fluid Mechanics 196, 467–494.

Patankar, S.V., Spalding, D.B., 1972. A calculation procedure for heat, mass and momentum transfer in three-dimensional parabolic flows. International Journal on Heat Mass Transfer 15, 1787–1806.

Roshko, A., 1954. On the development of turbulent wakes from vortex streets. NACA Report, 1191.

Sarpkaya, T., 1986. Force on a circular cylinder in viscous oscillatory flow at low Keulegan–Carpenter numbers. Journal of Fluid Mechanics 165, 61–71.

Stansby, P.K., Smith, P.A., 1991. Viscous forces on a circular cylinder in orbital flow at low Keulegan–Carpenter numbers. Journal of Fluid Mechanics 229, 159–171.

Tatauno, M., Bearman, P.W., 1990. A visual study of flow around an oscillating circular cylinder at low Keulegan–Carpenter numbers and low stokes numbers. Journal of Fluid Mechanics 211, 157–182.

Versteeg, H.K., Malalasekera, W., 1995. Computational Fluid Dynamics: The Finite Volume Method. Longman Scientific and Technical Press, UK.

Wang, C.Y., Dalton, C., 1991. Oscillating flow past a rigid circular cylinder: a finite difference calculation. Journal of Fluids Engineering 113, 377–383.

Wille, R., 1960. Kámán vortex streets. Advances in Applied Mechanics 6, 273–281.

Williamson, C.H.K., 1985. Sinusoidal flow relative to circular cylinders. Journal of Fluid Mechanics 155, 141–174.

Williamson, C.H.K., 1996. Vortex dynamics in the cylinder wake. Annual Review of Fluid Mechanics 28, 477–539.

Wu, G.X., Eatcok T.R., 1996. Transient motion of a floating body in steep waves. 11th Workshop on Water Waves and Floating Bodies, Hamburg.

Wu, G.X., Eatock, T.R., 2003. The coupled finite element and boundary element analysis of nonlinear interactions between waves and bodies. Ocean Engineering 30, 387–400.

Wu, G.X., Hu, Z.Z., 2004. Simulation of nonlinear interactions between waves and floating bodies through a finite element based numerical tank. Proceedings of the Royal Society London A 460, 2797–2817.

Wu, G.X., Sun, H., He, Y.S., 2004. Numerical simulation and experimental study of water entry of wedge in free fall motion. Journal of Fluids and Structures 19, 277–289.

Zhang, H.L., Zhang, X., 1997. Flow structure analysis around an oscillating circular cylinder at low KC number: a numerical study. Computers and Fluids 26, 83–106.